



In Situ Observation of Hard Surrounding Rock Displacement at 2400-m-Deep Tunnels

Xia-Ting Feng^{1,2} · Zhi-Bin Yao² · Shao-Jun Li¹ · Shi-Yong Wu³ · Cheng-Xiang Yang² · Hao-Sen Guo² · Shan Zhong¹

Received: 13 November 2016 / Accepted: 30 November 2017 / Published online: 6 December 2017
© Springer-Verlag GmbH Austria, part of Springer Nature 2017

Abstract

This paper presents the results of in situ investigation of the internal displacement of hard surrounding rock masses within deep tunnels at China's Jinping Underground Laboratory Phase II. The displacement evolution of the surrounding rock during the entire excavation processes was monitored continuously using pre-installed continuous-recording multi-point extensometers. The evolution of excavation-damaged zones and fractures in rock masses were also observed using acoustic velocity testing and digital borehole cameras, respectively. The results show four kinds of displacement behaviours of the hard surrounding rock masses during the excavation process. The displacement in the inner region of the surrounding rock was found to be greater than that of the rock masses near the tunnel's side walls in some excavation stages. This leads to a multi-modal distribution characteristic of internal displacement for hard surrounding rock masses within deep tunnels. A further analysis of the evolution information on the damages and fractures inside the surrounding rock masses reveals the effects of excavation disturbances and local geological conditions. This recognition can be used as the reference for excavation and supporting design and stability evaluations of hard-rock tunnels under high-stress conditions.

Keywords Deep hard-rock tunnel · Displacement · Time-dependent evolution · Spatial distribution · Fracture evolution

1 Introduction

Surrounding rock mass displacement induced by excavation in deep tunnels is fundamental information for adequately comprehending the failure development process under high-stress conditions. China's Jinping Underground Laboratory Phase II (CJPL-II) was established for investigating the physical properties and mechanics of rocks at a great depth of 2,400 m (Feng et al. 2016b). It provides a valuable site for keenly observing the displacement behaviour of deep hard rocks.

Previously, numerous researchers have adopted various methods to understand the displacement of hard rocks under high-stress conditions. Hibino et al. (1993), Hibino and Motojima (1995) analysed data gathered by multi-point extensometers as well as internal fracturing images obtained using a digital panoramic borehole camera; their results show that such displacements typically comprise two parts: 'opening displacement' of rock fractures and 'strain displacement' of intact rocks. Studies conducted at the Underground Research Laboratory (URL), Canada, (Martino and Chandler 2004) also showed that in highly stressed rocks, damage will develop around underground openings even when a low-energy excavation method is used. Five types of deformation zones, namely brittle joint zones, brittle fault zones, semi-brittle zones, low-grade ductile zones and high-grade ductile zones, were identified at the Olkiluoto site, Western Finland, by considering the geometry of the structures that form under a range of crustal conditions from brittle to ductile (Posiva 2009; Hudson et al. 2011). Malan (1998, 1999) considered that the time-dependent behaviour is the result of the rheology of the mining-induced fracture zone surrounding the excavations at depth. Andersson and Martin (2009, Andersson

✉ Xia-Ting Feng
Xia.ting.feng@gmail.com; xtfeng@whrsm.ac.cn

¹ State Key Laboratory of Geomechanics and Geotechnical Engineering, Institute of Rock and Soil Mechanics, Chinese Academy of Sciences, Wuhan 430071, China

² Key Laboratory of Ministry of Education on Safe Mining of Deep Metal Mines, Northeastern University, Shenyang 110819, China

³ Yalong River Hydropower Development Company, Ltd., Chengdu 610051, China

et al. 2009) studied the observations of the Äspö pillar stability experiment (APSE) and suggested that there appeared to be a well-defined boundary. If the stresses reached this boundary, yielding was observed; however, if the stresses were only slightly below this boundary, yielding or time-dependent processes were not observed. Wei et al. (2010) analysed that the proportion of displacement induced by rock damage increases under high geostress and within rock masses with a low compressive strength. Nadimi et al. (2011) considered that the in situ creep of a rock mass is governed by the behaviour of discontinuities. Huang et al. (2011) proposed that the time-dependent displacement characteristics of the surrounding rock mass can be considered with the gradual development of rock failure under high-geostress conditions. The outcome of the Posiva Olkiluoto Spalling Experiment (POSE) (Siren et al. 2015) concluded that rock failure mainly occurs owing to structurally controlled factors rather than being dictated solely by the expected location of the maximum stress. Zareifard and Fahimifar (2016) found that the effect of a damaged zone induced by excavation on the displacement may be significant.

Such investigations have induced significant progress in the understanding of displacement changes in deep tunnelling excavations, with particular focus on the effect of excavation and existing geological structures (mostly associated with weak structural planes) on the overall displacement magnitude. Moreover, for deep hard-rock tunnelling, stiff structures (such as pre-existing cracks) are the main features of local geological conditions and can considerably affect the failure of surrounding rock masses, e.g. rock bursts (Feng et al. 2015; Xiao et al. 2016). Hence, their influence on displacement levels should be strongly considered; however, such studies present little insight into the co-evolution process of displacement and rock mass damage due to the inherent difficulties of arranging an efficient monitoring system. With increased geostress levels, the failure modes of hard-rock masses may drastically change (Hoek and Brown 1980). Currently, displacement-monitoring equipment is mostly installed after the excavation of the observation sections, usually resulting in the loss of important evolution information induced by excavation. In addition, displacement data are usually collected via manual readings at intervals of days or weeks. Acquisition frequencies are typically too low to attain accurate displacement evolution characteristics during the excavation process.

In this study, a more comprehensive monitoring system that includes pre-installed multi-point extensometers with continuous-recording techniques, acoustic velocity testing and digital borehole camera systems is employed in tunnels with depths of ~ 2,400 m at CJPL-II to capture the entire spatial and temporal evolution process of excavation-induced displacement. The co-evolution mechanisms of

displacement and excavation damage with the fracturing of deep hard rocks are systematically discussed to reveal the effects of excavation disturbances and local geological conditions.

2 Background of CJPL-II

2.1 Geological Conditions

CJPL-II, with its maximum depth of ~ 2,400 m, lies to the south of the traffic auxiliary tunnel A between the chain-ages AK7+600 and AK8+150 at the Jinping II hydropower station (Feng et al. 2016a). It includes four traffic tunnels and nine laboratory tunnels, as shown in Fig. 1. The entire project is located in an anticline zone denoted by a near-NS trend axis, with the axis of the 2# access tunnel lying along the core of the anticline and the 1#-3# Labs and 4#-8# Labs situated in the NW and SE flanks of the anticline, respectively. In the project region, two long and extended fault zones with maximum widths of ~ 1 m are found in the 2#-4# Labs and they intersect the anticline on the whole. According to a geological structure survey and field investigation, the surrounding rock mass can be divided into two zones. Zone I comprises the core area of the anticline and the fault fracture zone, and Zone II includes the two flank areas of the anticline, as shown in Fig. 1. Generally, the natural fractures in this region are undeveloped. Herein, three main sets of fractures are observed. ① N81°W NE∠74°: the fractures in this set are parallel to each other and intermittent. Moreover, their extended length is short, and the fracture spacing is generally within the range of 20–40 cm. This value can be in the range of 5–10 cm in localised areas. The fractures in this set are smooth and filled with cataclastic rocks; in addition, water can be observed to ooze from the fracture surface. ② N28°W NE∠70°: the fractures in this set are also parallel and intermittent; however, their average extended length is longer than that of the fractures in the first set. The fractures in this set are straight and filled with debris and calcium coating. In addition, slight corrosion and water-dripping can be observed on the fracture surface. ③ N51°E NW∠70°: this set comprises bedding fractures. The thickness of a single bed is greater than 1 m, and the extended length of the fractures is very long.

The results of in situ stress obtained using the stress relief method in the connectivity tunnel between the 6# and 7# Labs show that the maximum and intermediate principal stresses are about 70 MPa and the minimum principal stress is about 25 MPa, which indicates extremely high stress. The directions of the three principal stresses are NW, SSE and NEE respectively, i.e. the maximum and intermediate principal stresses are at a small angle with the tunnel axis, and the minimum principal stress

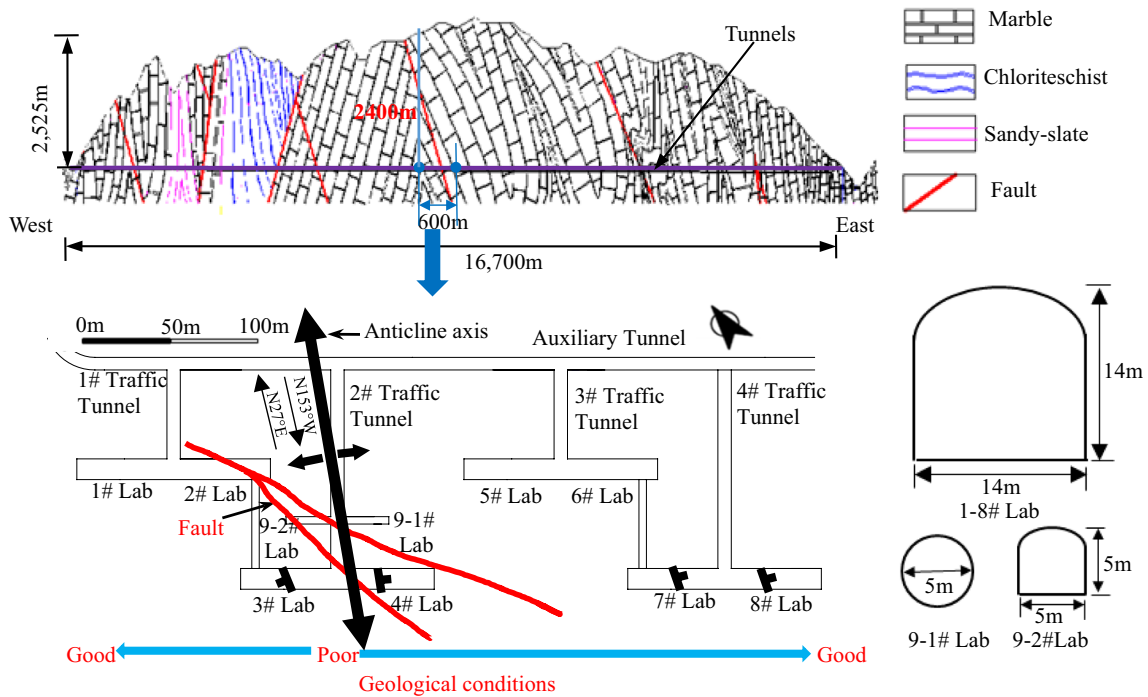


Fig. 1 Profile of CJPL-II (modified from Feng et al. 2016a, b)

is almost perpendicular to the tunnel. The main stratum at the construction site is Triassic marble belonging to the Baishan Group (T2b) and varies significantly at different laboratory locations. The cores obtained from the borehole in the monitoring section of the 1#, 2#, 4# and

5# Labs are shown in Fig. 2, and the features and mechanical parameters of those cores are shown in Table 1. The uniaxial compressive strength of this marble ranges from 60 to 190 MPa, and its Young’s modulus ranges from 30 to 50 GPa. In the entire project area, the integrity of rock

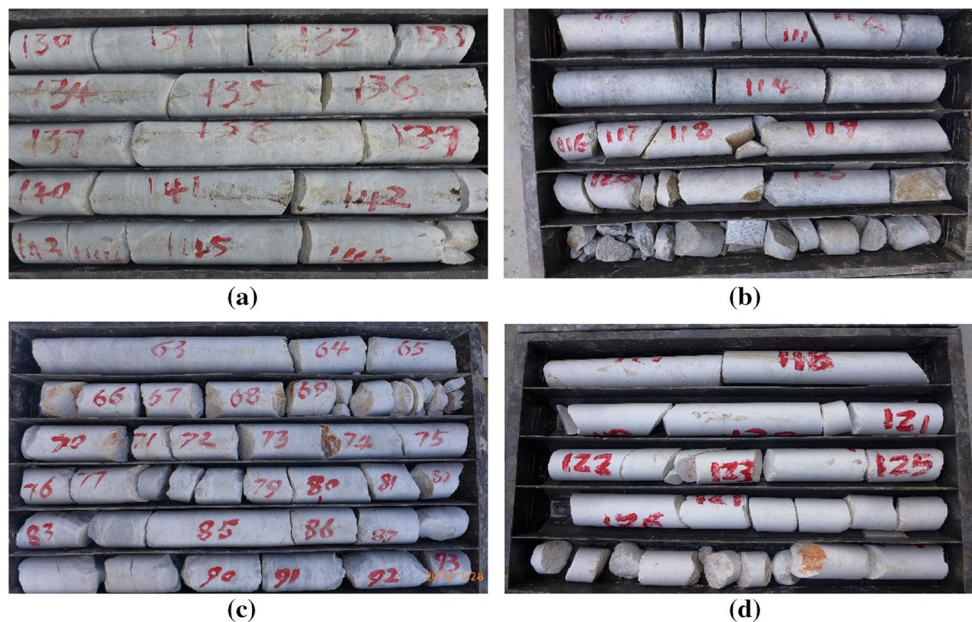


Fig. 2 Rock cores from borehole: a 1# Lab, b 2# Lab, c 4# Lab, d 5# Lab

Table 1 Rock features and mechanical parameters

Location	Features	Uniaxial compressive strength (MPa)	Young's modulus (GPa)
1# Lab	Black and grey marble with white strip or slab	180–190	40–50
2# Lab	Grey and white marble	80–120	34–45
4# Lab	Weathering	60–120	30–40
5# Lab	Grey and white marble	80–120	35–45

masses is poorest in the #3 and #4 Labs and improves gradually from the core to both anticline flanks.

2.2 Tunnel Configuration and Excavation Methods

On the whole, the testing tunnels were constructed in marble with staggered sequences, as shown in Fig. 1. The profiles of the tunnels are shown in Fig. 1, with a length of 65 m and a 14 m × 14 m cross-section for 1#–8# Labs. The 9# Lab is divided into two segments, namely 9-1# and 9-2#, and each segment has 30 m length and cross-section of 5 m × 5 m or ϕ 5 m.

Using the drill and blast method, the 1#–8# Labs were excavated in layers and steps. The upper layer, 8.5 m high, was excavated in two steps: excavation of pilot tunnels (Step I) and slashing excavation of side walls (step II) with a 3-m excavation footage. The pilot tunnel was excavated first from the centre line of the access tunnel to the end of each laboratory, whereas slashing excavation was conducted in the

opposite direction. Similarly, for the 1#–3# and 5#–8# Labs, which had a 5.5-m-high bench, excavation was performed in two steps: excavation of the middle groove (Step III) and slashing excavation of the side walls (Step IV) at an advance speed of ~ 5 m per day, as shown in Fig. 3a. For the 4# Lab, the 2-m-high middle layer was excavated first (Step III), followed by the 3.5-m-high bottom layer (Step IV), as illustrated in Fig. 3b. Millisecond blasting was adopted and the typical blasting design and blasting parameters are shown in Fig. 4 and Table 2, respectively. The design may be slightly adjusted according to geological conditions.

Located in highly stressed areas, rock burst and the associated stress-induced damage will generally appear primarily because of instant unloading and subsequent stress redistribution. In most areas, the damage degree mainly ranges from slight to moderate and the damage depth is less than 2 m. Strong and extremely strong rock localised failures may occur in areas wherein the damage depth is usually greater than 2 m. The tunnels are supported using shotcretes, prestressed rock-bolts and steel meshes (Huadong Engineering Corp. Ltd. 2014), as shown in Fig. 5a. Depending on the survey result for the working face and walls, strengthening supports with 9-m-long rock-bolts and steel arch ribs are adopted in areas wherein the rock masses are heavily fractured (e.g. the 3# and 4# Labs) or severely damaged owing to rock burst (e.g. the 7# and 8# Labs), as shown in Fig. 5b.

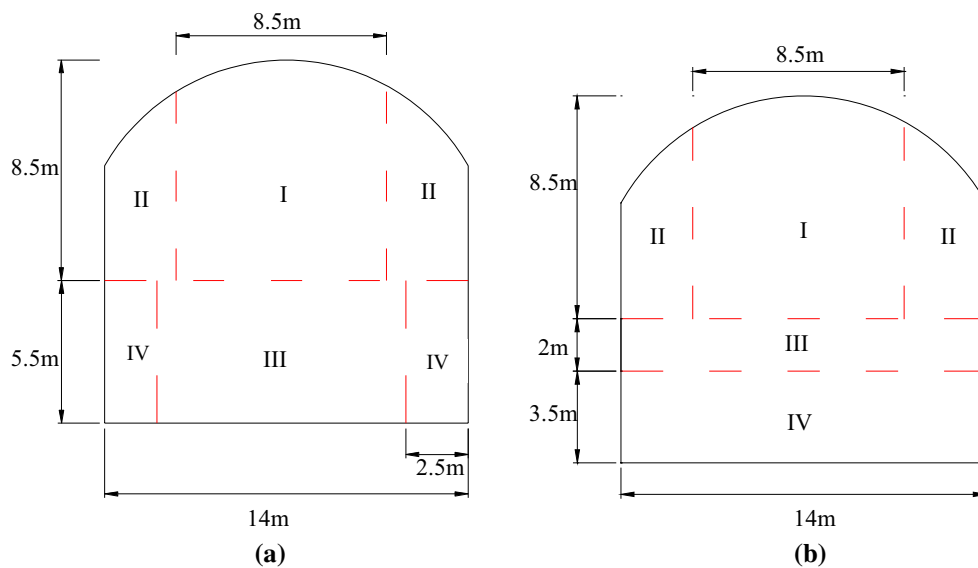


Fig. 3 Excavation sequences for the laboratories: **a** The 1#, 2#, and 5# Lab (step I: middle pilot tunnel, step II: side wall in the upper layer, step III: middle groove, step IV: side wall in the bottom layer),

b The 4# Lab (step I: middle pilot tunnel, step II: side wall in the upper layer, step III: medium layer, step IV: bottom layer)

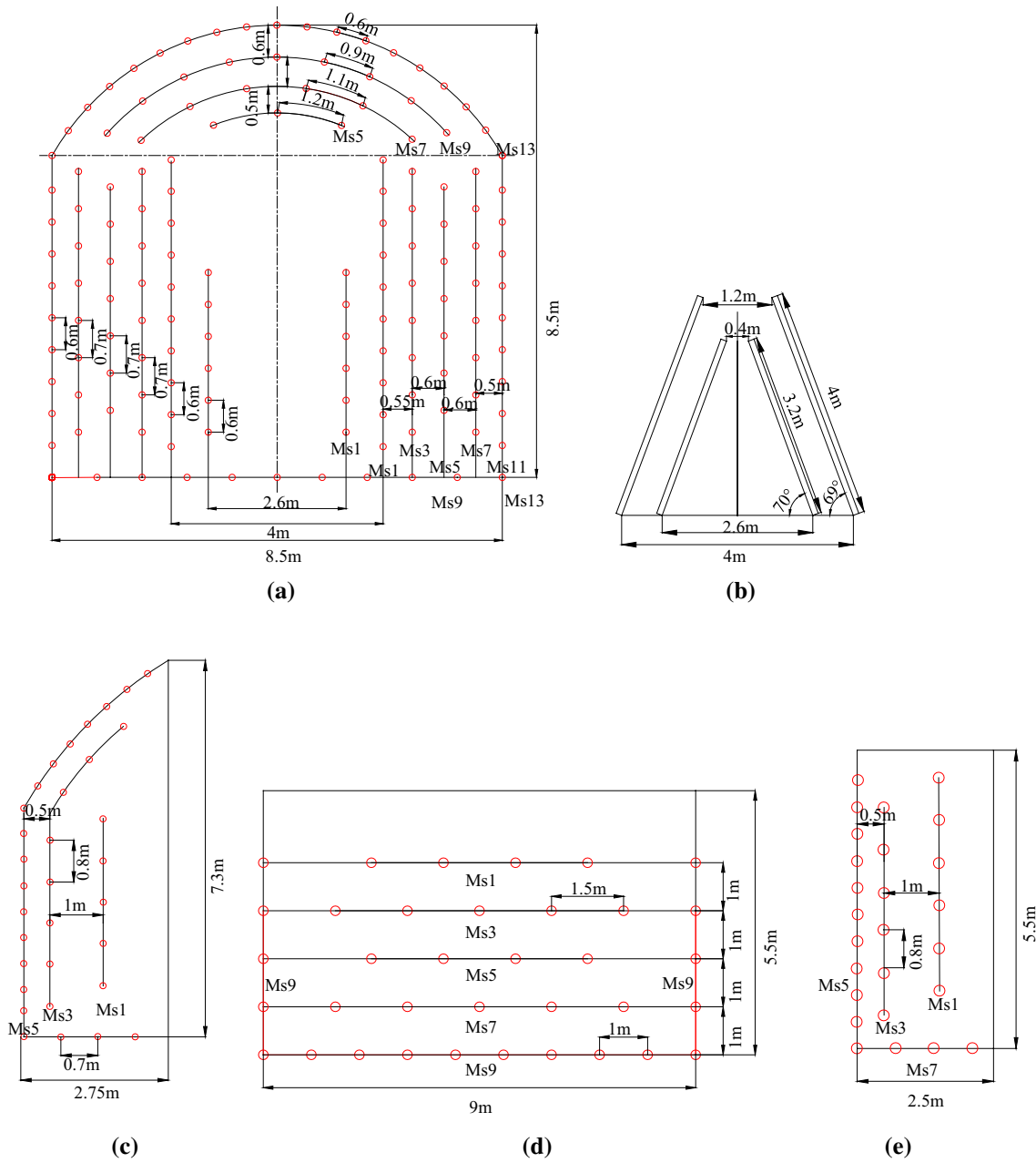


Fig. 4 Layout of the blasting holes: **a** Step I, **b** cutting holes (MS1) during step I, **c** step II, **d** step III, **e** step IV

Table 2 Excavation blasting parameters

Excavation step	Advance-ment length (m)	The number of blast holes	The length of blast holes (m)	Delay subdivi-sion	The maximum charge per detonating period (kg)	The charge amounts (kg)
I	3	140–146	3.2–4	7	74	234
II	3	34–37	3.5	3	21	41
III	5	36–40	5	5	30	108
IV	5	24–28	5	4	13	47

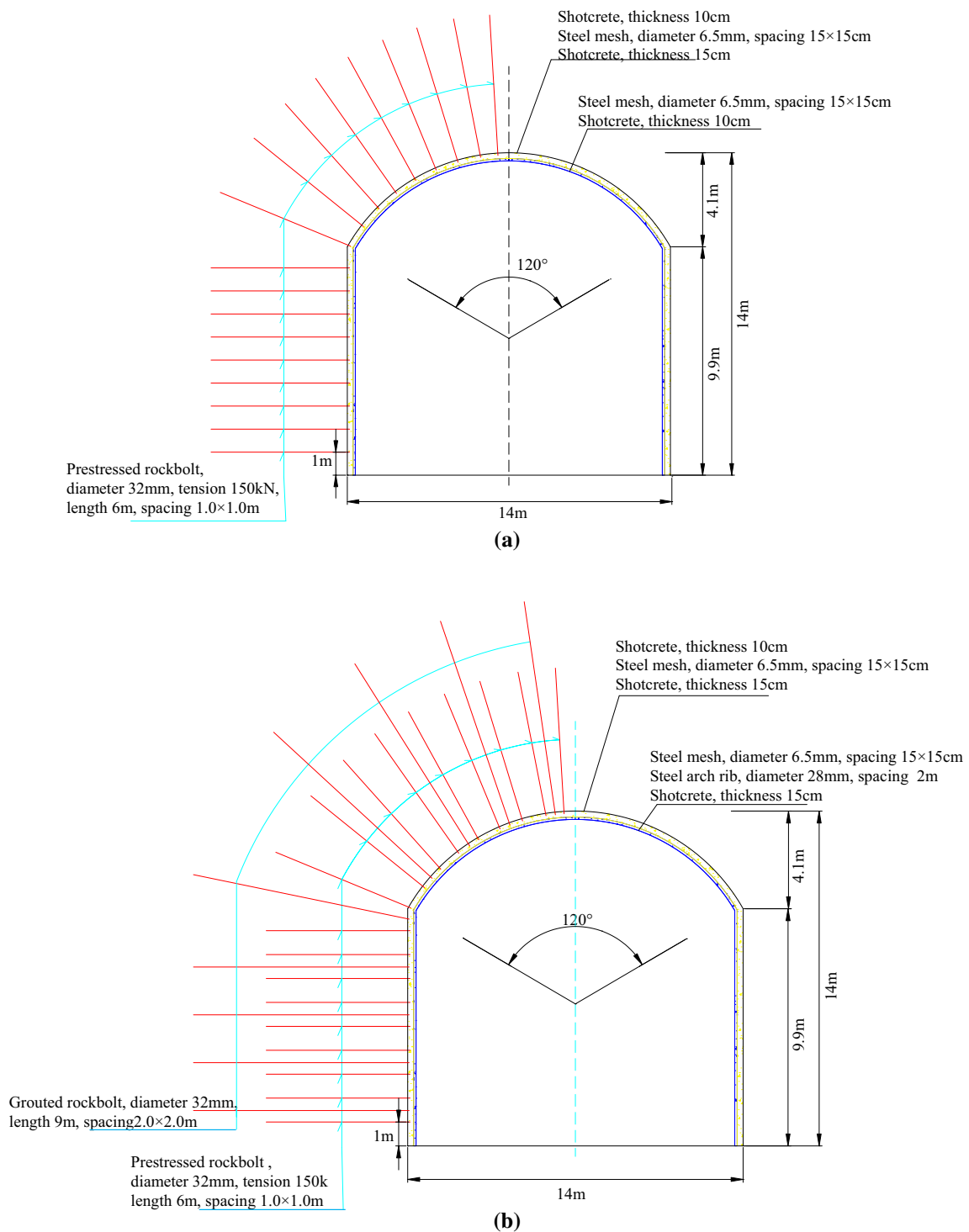


Fig. 5 Support system: **a** conventional support, **b** strengthening support (Huadong Engineering Corp. Ltd. 2014)

3 Comprehensive Monitoring Scheme

A comprehensive monitoring scheme was adopted to capture the co-evolution of the internal displacement, geological structure and excavation damage zones of surrounding rock

masses. Three associated monitoring approaches, namely multi-point extensometers, digital borehole cameras and acoustic velocity testing, were ultimately employed as per the methods suggested by the International Society for Rock Mechanics (ISRM) (Hansmire 1978; Li et al. 2013;

Takahashi et al. 2006). To study the influences of different geological conditions, five sets of identical multi-point extensometers (BKG-A3, produced by China Geokon Instruments Co. Ltd.), named as the DSP series, were installed in different laboratories; they covered the typical local geological features shown in Fig. 1. Meanwhile, four boreholes for performing digital borehole camera photography and acoustic velocity testing, named as the CAP series, were drilled near the DSP boreholes, as illustrated in Fig. 6.

Prior to the excavation of the laboratories, seven boreholes, each with a length of 60 m, were drilled from the auxiliary tunnel to the testing laboratories. Four multi-point extensometers were installed before the excavation of the testing laboratories, denoted as DSP-01-T, DSP-01-M, DSP-02 and DSP-03, respectively. As shown in Fig. 7a, five measurement points (i.e. A, B, C, D and E) were fixed in the subject boreholes using cement mortar, with O as the fixed end. DSP-01-M and DSP-02 were set on the side wall of the bottom layer, with point A lying at a distance of 0.5 m from the side wall. DSP-01-T and DSP-03 were set in the spandrel of the laboratory. The distances between the side wall and the measurement points DSP-01-T-A and DSP-03-A were 1.5 m and 2.5 m, respectively. The boreholes CAP-01, CAP-02 and CAP-03 were arranged parallel to and 2-m away from the boreholes DSP-01-T, DSP-02 and DSP-03, respectively. In addition, DSP-04 and CAP-07, each with a length of 30 m, were drilled from the 9-1# Lab to the unexcavated 4# Lab. The arrangement of the measurement points in DSP-04 is shown in Fig. 7b.

Before the installation of the multi-point extensometers, the results of the digital borehole camera testing and acoustic velocity testing of the DSP boreholes were analysed to obtain the original geological informative data. During the excavation process, the multi-point extensometers used for measuring the internal displacements in the surrounding rock mass were programmed to automatically record data

every 10 min. Simultaneously, digital borehole camera observations and acoustic velocity testing were routinely performed in the CAP boreholes to obtain information about the damage and fracture evolution of the surrounding rock mass. Because the CAP and DSP boreholes were parallel and at the same elevation, within a distance of 2 m, the geological conditions between the two boreholes can be considered to be virtually identical (Fig. 8). Therefore, the extent of damage and fracture in the CAP boreholes can be used to evaluate the same in the DSP boreholes.

4 Time-Dependent Evolution Characteristics of the Internal Displacement in Surrounding Rock Masses

4.1 Time-Dependent Evolution Characteristics

Typical measurements of the internal displacements in the surrounding rock masses during the entire excavation process are shown in Fig. 9. By analysing the displacement evolution characteristics at each measurement point, four types of displacement-increasing modes associated with the excavation process were observed: (1) displacement increased abruptly at every excavation blasting but showed no change during two adjacent blasts (i.e. displacement regularly exhibited a step-shaped increase with the excavation process, named as ‘S-type’ for convenience, as illustrated in Fig. 10a); (2) displacement showed a sharp increase at every blasting and then a time-dependent continuous increase during two adjacent blasts, denoted as ‘C-type’, as shown in Fig. 10b); (3) with the working face advancing towards the monitoring section, the displacement at some measurement points first showed S-type characteristics, then C-type tendencies and finally converted back to the S-type after the working face passed the monitoring section (ultimately

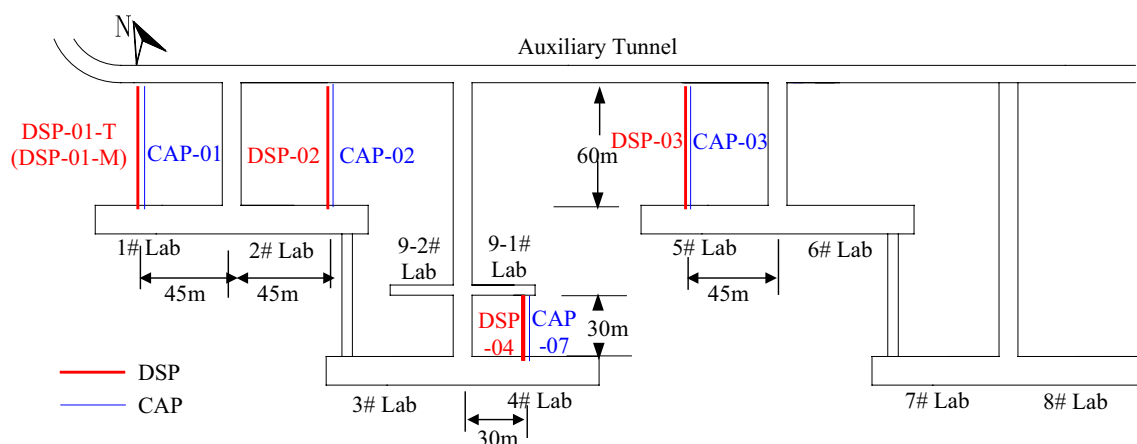


Fig. 6 Layout of multi-point extensometers and testing boreholes

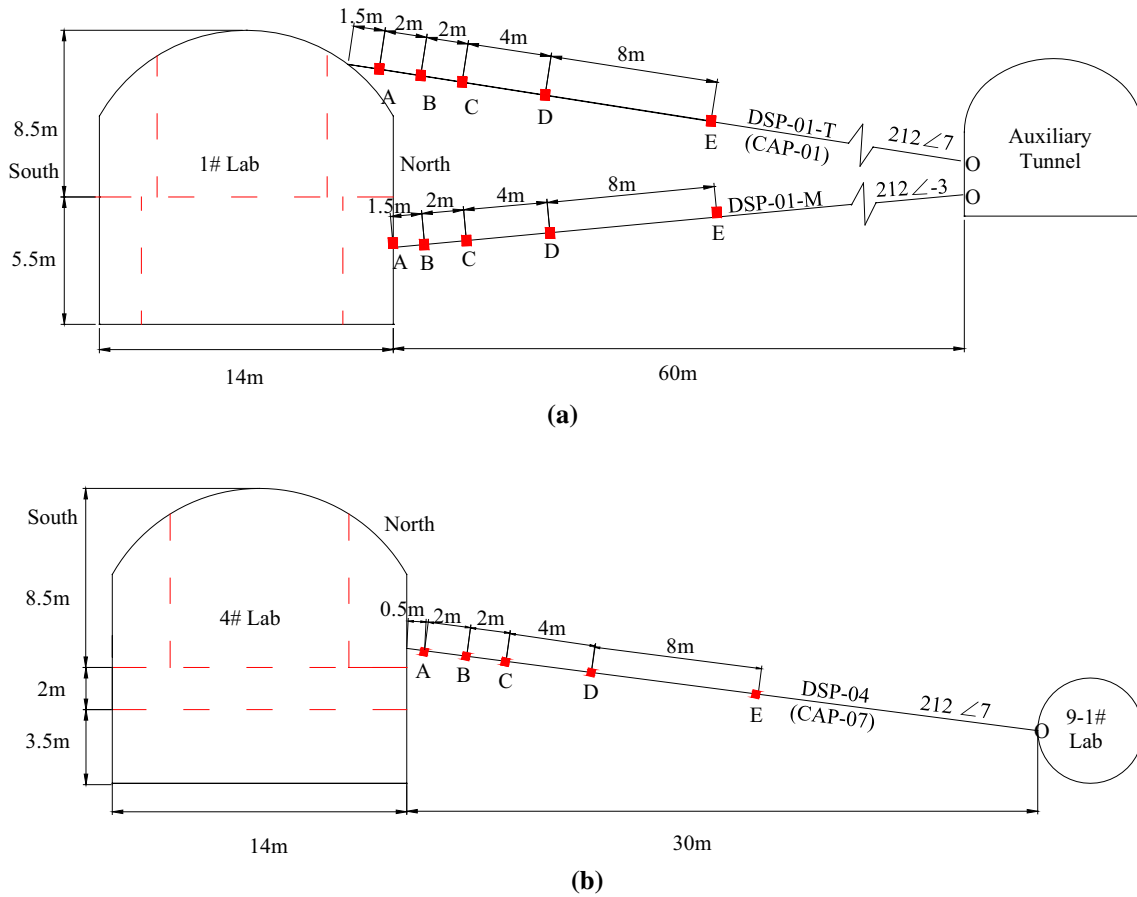


Fig. 7 Typical arrangement of the multi-point extensometers: a DSP-01-T and DSP-01-M, b DSP-04

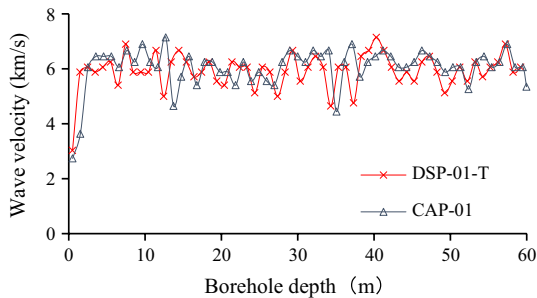


Fig. 8 Comparison of acoustic velocity test results in DSP-01-T and CAP-01 boreholes

denoted as ‘S–C–S-type’), as illustrated in Fig. 10c and (4) displacement at some points remained C-type when the working face passed the monitoring section (denoted as ‘S–C-type’), as illustrated in Fig. 10d. The types of displacement evolutions for different measurement points are summarised in Table 3.

4.1.1 Evolution Characteristics of S-Type Displacements

S-type displacements occurred at most of the measurement points of DSP-01-T, DSP-01-M, DSP-02 and DSP-03 during the excavation of the upper layer as well as at points D and E during the excavation of the bottom layer. Taking DSP-01-T as an example, the displacement evolution during the excavation of the upper-middle pilot tunnel is shown in Fig. 11. In addition, Fig. 12 shows the corresponding testing result obtained from the digital borehole camera at CAP-01 before and after the excavation of the upper-middle pilot tunnel.

According to Fig. 12, the fractures mainly evolved within a range of 1.5 m, forming an excavation-damaged zone (EDZ) with a depth of 2 m after the excavation of the upper-middle pilot tunnel. Given that the measurement point DSP-01-T-A was located 2.3 m from the boundary of the middle pilot tunnel, measurement points A–E were ultimately outside the range of the fracture evolution area and EDZ, i.e. there were no pre-existing cracks or cracking where the displacement was an S-type displacement. Similar

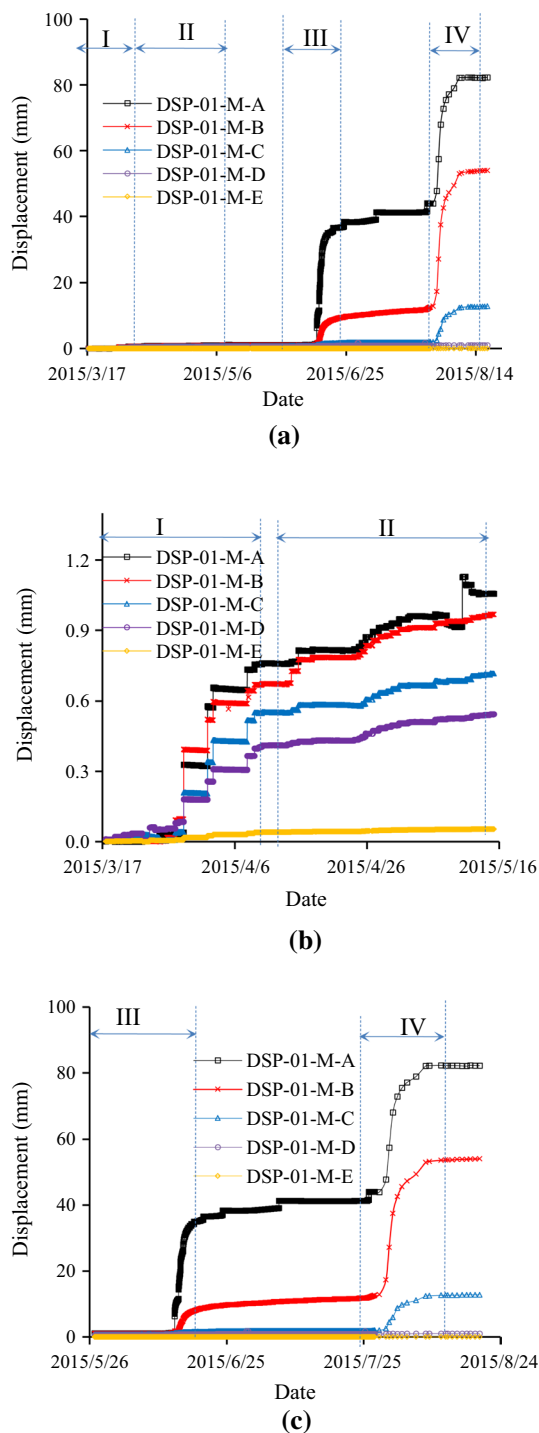


Fig. 9 Displacement evolution at measurement points DSP-01-M: **a** the whole excavation process, **b** excavation of the upper layer, **c** excavation of the bottom layer

results were evident for the other measurement points that were characterised as S-type.

4.1.2 Evolution Characteristics of C-Type Displacements

The evolution of C-type displacements was typically observed at DSP-04-A in the 4# Lab (Fig. 13). The displacement here increased almost in C-type during the entire excavation period. The fracture distribution in DSP-04 is shown in Fig. 14; for CAP-07, the fracture evolution before and after the excavation of the upper layer is shown in Fig. 15.

According to Fig. 14, the fractures in DSP-04 were more developed. As shown in Fig. 15, the pre-existing cracks opened and a series of new cracks formed within a range of 4 m from the side wall. The fractured rock masses appeared to be very sensitive to even small disturbances. Thus, the subject displacement continued to increase and displayed a time-dependent behaviour during the later period of stress redistribution between two adjacent excavation blasts.

4.1.3 Evolution Characteristics of S-C-S-Type Displacements

This type appeared at measurement points DSP-01-T-B, DSP-01-M-A, DSP-02-A and DSP-02-B during the excavation of the bottom layer’s middle groove. In addition, the displacement at DSP-02-B was of this type during the excavation of the bottom layer’s side wall.

For example, the displacement at measurement point DSP-02-A (Fig. 16) was of S-type when S_{III} , the distance between the monitoring section and the working face of the bottom layer’s middle groove, was less than -1 m (‘-’ signifies that the working face was in front of the monitoring section). Subsequently, the displacement was of the C-type when S_{III} ranged from -1 to 9 m. As the working face advanced, when S_{III} was greater than 9 m, the displacement was S-type again.

Figure 17 shows the results obtained from the digital borehole camera and acoustic velocity testing at CAP-02 before and after the excavation of the middle groove in the 2# Lab. The fracture evolution area was mainly found within a range of 1.5 m from the boundary, and the depth of the EDZ was 3 m. By this time, DSP-02-A was at a distance of 2.3 m from the boundary. Although no distinct fracture evolution was observed around DSP-02-A, the apparent decrease in the wave velocity indicates the degradation of the rock mass, which can be attributed to blasting damage. When the working face approached, the measurement point was strongly influenced by the excavation disturbance, followed by the presence of a C-type displacement. In contrast, when the working face advanced to a considerable distance, the displacement reverted to the S-type.

Fig. 10 Types of displacement evolution characteristics: **a** S-type, **b** C-type, **c** S–C–S-type, **d** S–C-type

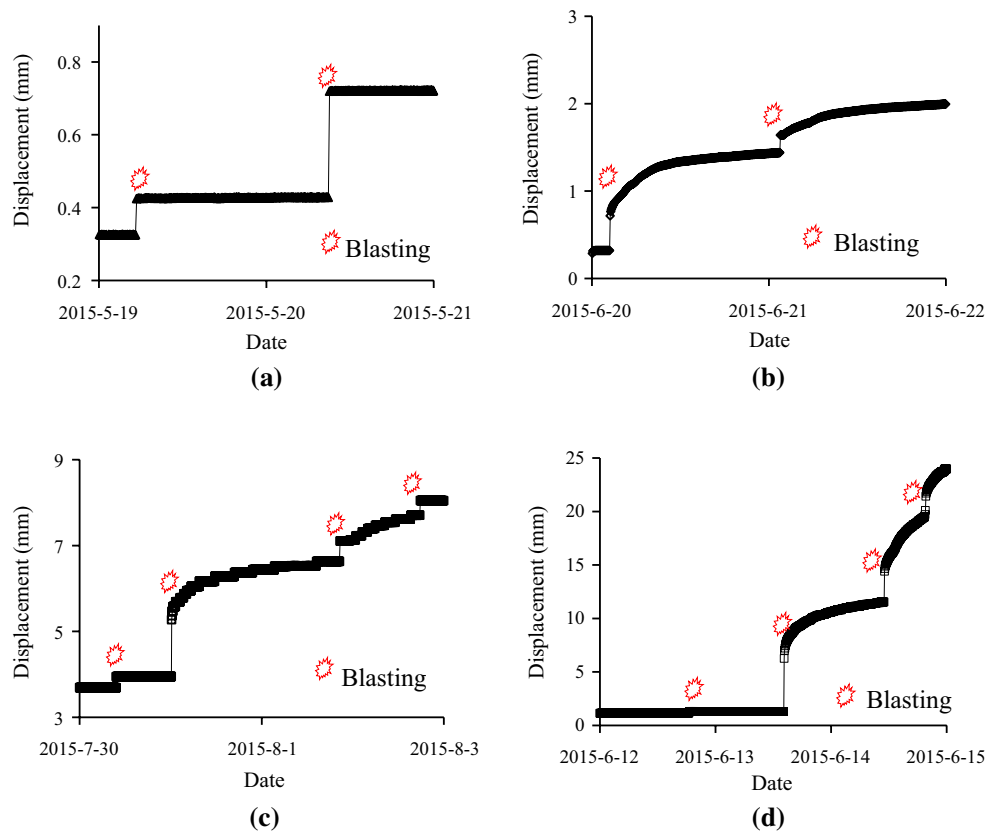


Table 3 Types of displacement evolution characteristics at measurement points for different excavation sequences

Location	Multi-point extensometers	Measuring points	Types of displacement evolution characteristics			
			Step I	Step II	Step III	Step IV
1# Lab	DSP-01-T	A	S	/	/	/
		B	S	S	S–C–S	/
		C	S	S	S–C–S	/
		D	S	S	S	/
		E	S	S	S	/
	DSP-01-M	A	S	S	S–C–S	/
		B	S	S	S–C	/
		C	S	S	S	/
		D	S	S	S	/
		E	S	S	S	/
2# Lab	DSP-02	A	S	S	S–C–S	S–C
		B	S	S	S–C–S	S–C–S
		C	S	S	S	S
		E	S	S	S	S
4# Lab	DSP-04	A	S–C	C	C	Outrange
		B	/	/	C	C
		D	S–C	C	C	C
		E	S–C	C	/	/

“/” denotes that the measurement point was damaged or data were not collected automatically in the process

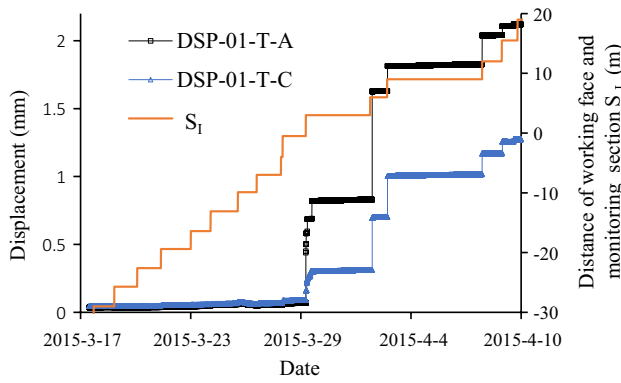


Fig. 11 Displacement evolution at measurement points DSP-01-T-A and DSP-01-T-C during the excavation of middle pilot tunnels in 1# Lab (S_I is the distance between the monitoring section and the upper pilot working face)

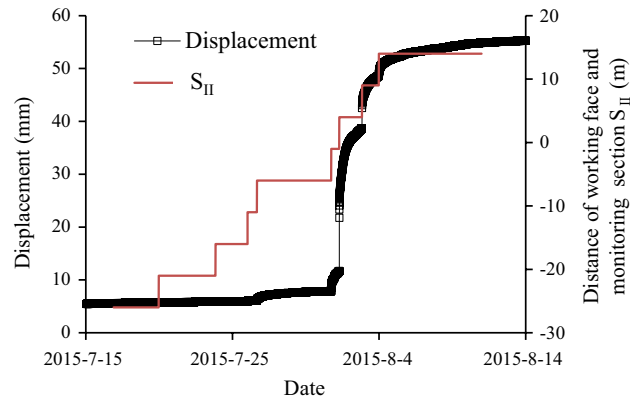
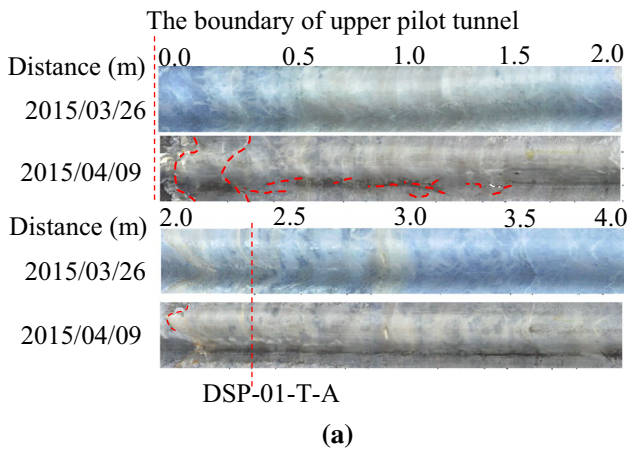
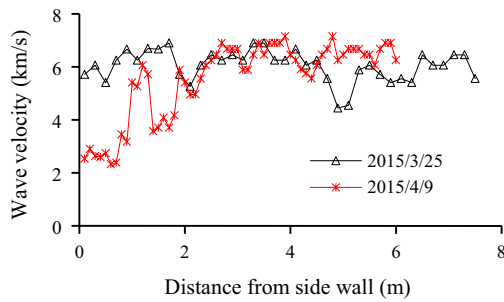


Fig. 13 Displacement evolution at point DSP-04-A during the excavation of upper side wall in 4# Lab (S_{II} is the distance between the monitoring section and the working face of upper side wall)



(a)



(b)

Fig. 12 Comparisons of test results in CAP-01 before, and after the excavation of the upper layer in 1# Lab: **a** Borehole images of fracture evolution, **b** changes in elastic wave velocity

4.1.4 Evolution Characteristics of S–C-Type Displacements

The evolution of S-C-type displacements was observed at measurement point DSP-01-M-B during the excavation of the middle groove in the 1# Lab and at DSP-02-A during the expanding excavation of the bottom layer’s side wall in the

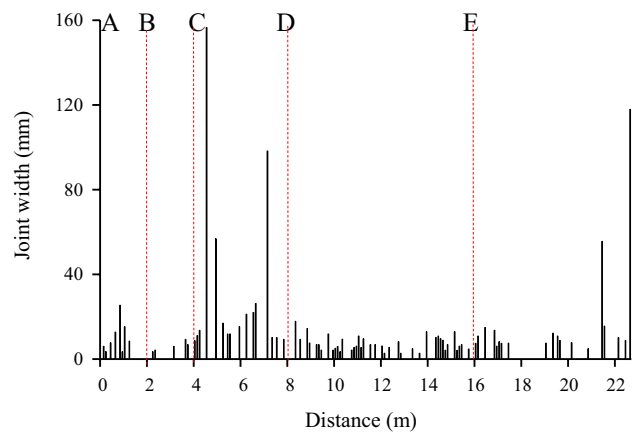


Fig. 14 Fracture distribution in DSP-04 before the excavation (A, B, C, D and E are measurement points)

2# Lab. As shown in Fig. 18, taking DSP-02-A for example, the displacement was of the S-type and C-type when the working face was located ahead and behind the monitoring section, respectively.

The fracture evolution in CAP-02 before and after the expanding excavation of the side wall in the bottom layer is shown in Fig. 19. On 12 August 2015, the working face passed the monitoring section of DSP-02. At that moment, DSP-02-A was in the fracture evolution area; accordingly, the displacement of DSP-02-A changed to C-type.

4.2 Analysis of the Mechanism of Internal Displacement Evolution in Surrounding Rock Masses

The evolution characteristics of displacements in hard-rock tunnels are primarily affected by rock mass integrity.

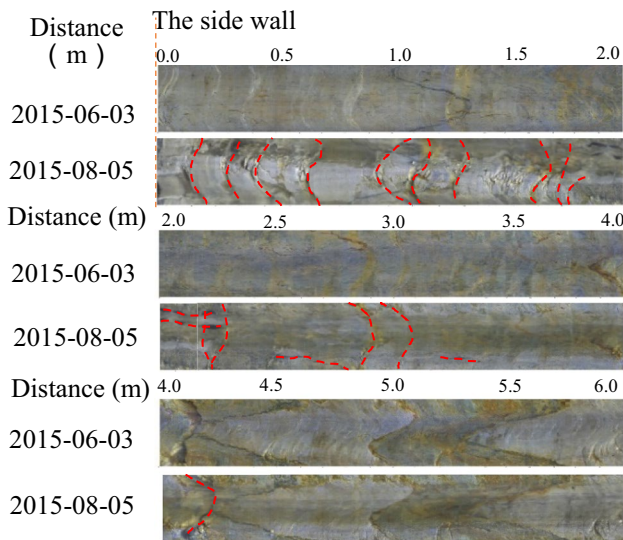


Fig. 15 Comparison of borehole images of CAP-04 before, and after the excavation of upper layer

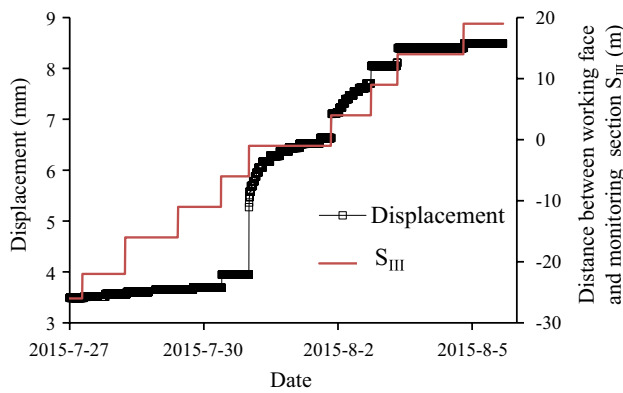
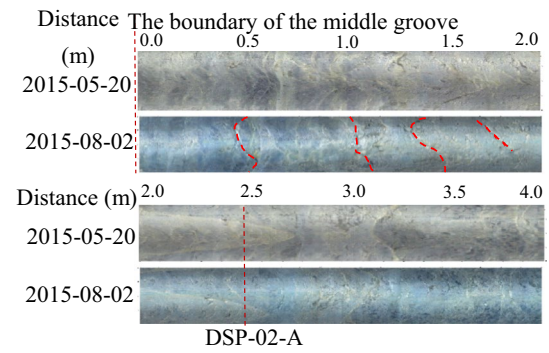
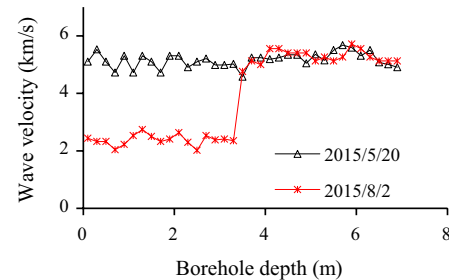


Fig. 16 Displacement evolution at measurement point DSP-02-A during the excavation of middle groove in 2# Lab (S_{III} is the distance between the monitoring section and the working face of the middle groove)

Evolution of pre-existing cracks leads to time-dependent behaviour even under mild excavation disturbance conditions. Table 4 summarises a comparison of densities and average widths of pre-existing cracks in DSP boreholes, total displacement amounts and proportion of C-type displacements. It can be seen that both the density and average width of the cracks in DSP-04 were the largest; meanwhile, the displacement of DSP-04 was of the C-type during almost the entire excavation process. In addition, its total displacement was largest. Owing to the enhanced geological conditions, DSP-02 presented a lower total displacement with a relatively smaller preponderance of the C-type, nevertheless still accounting for 69.63% of the displacement. Therefore, it can be asserted that the weaker the rock mass integrity, the



(a)



(b)

Fig. 17 Comparison of test results in CAP-02 before, and after the excavation of the middle groove in 2# Lab: **a** Borehole images of fracture evolution, **b** Changes in elastic wave velocity

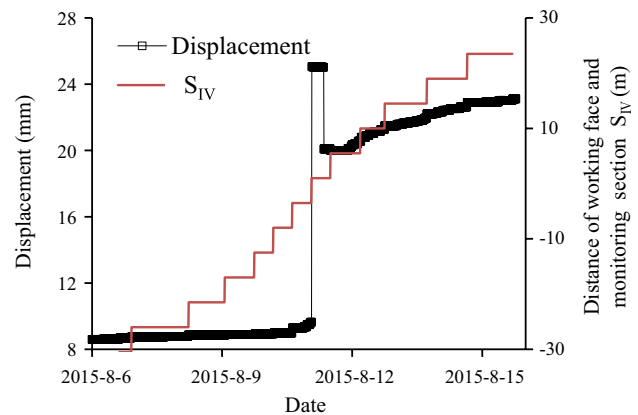


Fig. 18 Displacement evolution at measurement point DSP-02-A during the excavation of bottom side wall in 2# Lab (S_{IV} is the distance between the monitoring section and the working face of bottom side wall middle groove)

greater the percentage of C-type displacement and the larger the total displacement.

On the other hand, excavation damage plays an important role if the rock mass has robust integrity. Strong excavation may induce macro-cracks, as seen in the results obtained from the digital borehole camera. These macro-cracks will function similarly to the abovementioned pre-existing

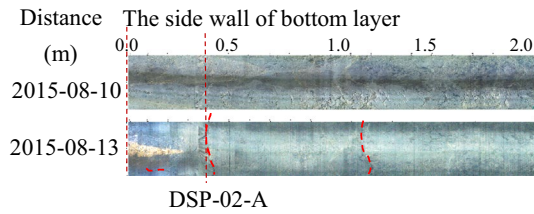
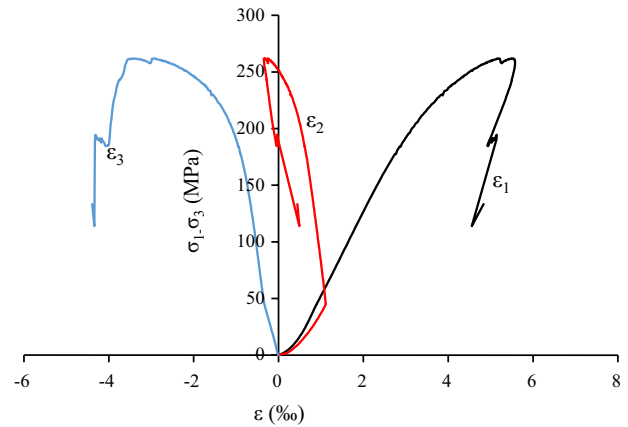


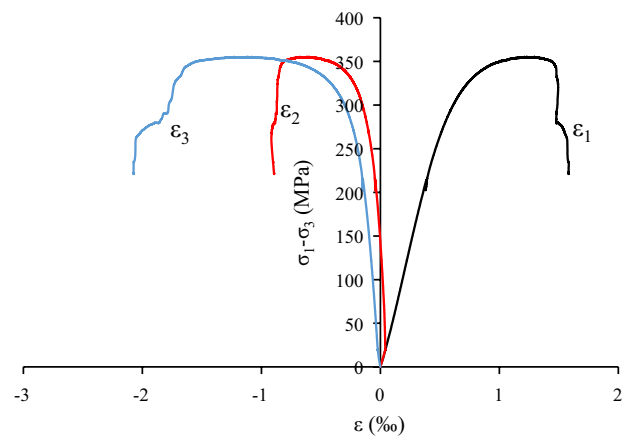
Fig. 19 Comparison of borehole images of CAP-02 before, and after the expanding excavation of the bottom side wall in 2# Lab

cracks, resulting in C-type displacement. In this case, with the working face advancing through the observation section, the displacement ultimately converts from S-type to S–C-type. If the excavation is not sufficiently forceful, relatively weak excavation damage with blast-induced micro-cracks (as detected by acoustic velocity testing) can also lead to C-type displacement. However, this typically happens when adjacent working faces are very close (i.e. when the excavation disturbance is quite strong). In these cases, the displacement is conventionally of the S–C–S-type with the working faces approaching, passing through and ultimately stepping away from the observation section. As a result, the displacements at measurement points located far away from the side wall, such as D and E, were of the S-type during the entire excavation process. In contrast, the displacements at measurement points near the side wall, such as A and B, were of the S-type at first; then, they showed C-type characteristics after the working face passed. This is because the farther the points are located from the side wall, the lesser the affected disturbance from the excavation. Moreover, because the pilot tunnel of the upper layer advanced with a step size of 3 m and the bottom layer advanced 5 m per step, the measurement points were affected more notably by the excavation of the bottom layer (according to the results obtained from the digital borehole camera and acoustic velocity testing). Therefore, S-type displacement evolution generally occurred during the excavation of the upper layer, and a number of C-type displacements generally occurred during the excavation of the bottom layer, with the specific displacement types being the S–C-type or S–C–S-type.

Third, the stress state has clear effect on the evolution of displacement. True triaxial tests of the marble in the 5# Lab were conducted based on the in situ stress state and stress



(a)



(b)

Fig. 20 Stress–strain curves of rocks from 5# Lab obtained by true triaxial tests: **a** $\sigma_2 = 50$ MPa, $\sigma_3 = 5$ MPa, **b** $\sigma_2 = 50$ MPa, $\sigma_3 = 30$ MPa

adjustment path. The marble showed brittle behaviour at low minimum principal stresses (e.g. $\sigma_3 = 5$ MPa in Fig. 20a) and ductile–brittle behaviour at high minimum principal stresses (e.g. $\sigma_3 = 30$ MPa in Fig. 20b). This explains why four types of in situ monitored displacement appear in Fig. 10. When the working face approached the monitoring sections, the stresses inside the rock mass gradually increased. When the distance was sufficiently large, the stress state remained in the elastic range, producing to instantaneous elastic

Table 4 Relationship between the geological conditions and the displacement characteristics

Multi-point extensometers	The density of pre-existing cracks (m^{-1})	The average width of pre-existing cracks (mm)	The percentage of the displacement increased in ‘C’ type to its total value (%)	Displacement (mm)
DSP-01-M	1.85	8.38	84.15	82.23
DSP-02	1.68	5.48	69.63	24.55
DSP-04	2.73	15.55	98	110

behaviour in the rock mass and an S-type displacement curve (e.g. DSP-01-T-A and DSP-01-T-C shown in Fig. 11). When the working face passed through the monitoring section, a part of the measuring points began to enter the stress concentration region. The rocks surrounding the excavation boundary were in a low confinement environment due to excavation-induced unloading, in which brittle fracturing and plastic damage occur, whereas the rock masses within a certain range in the interior were under ductile–brittle stress (e.g. point DSP-02-A, with S_{III} being within the range – 6–9,

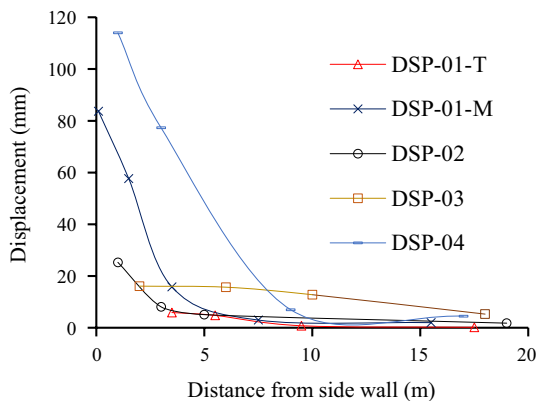


Fig. 21 Distribution of the final displacements at the measuring points after excavation

as shown in Fig. 16). This produced time-dependent evolution of displacement and a C-type curve. The rock masses far from the side wall remained in the elastic state and exhibited S-type displacement (e.g. points D and E in 1# and 2# Lab, as shown in Table 3). When the working face had exited the monitoring section, the rock masses in the severely damaged zone exhibited rheological and time-dependent characteristics, and the displacement evolution curve showed C-type evolution (e.g. DSP-02-A, as shown in Fig. 18). This is similar to the fractured rock mass. The rock masses near the area that were once at the ductile–brittle stress level may return to the elastic state, so that the displacement evolution was once more of the S-type (e.g. DSP-02-A, with S_{III} exceeding 19, as shown in Fig. 16).

5 Spatial Distribution of the Internal Displacement in Surrounding Rock Masses

5.1 Spatial Distribution Characteristics

As shown in Fig. 21, after the excavation, the displacement in different areas or at different depths from sidewall varies significantly. Owing to the differences in the lithology and geological conditions, the displacement and the influence of

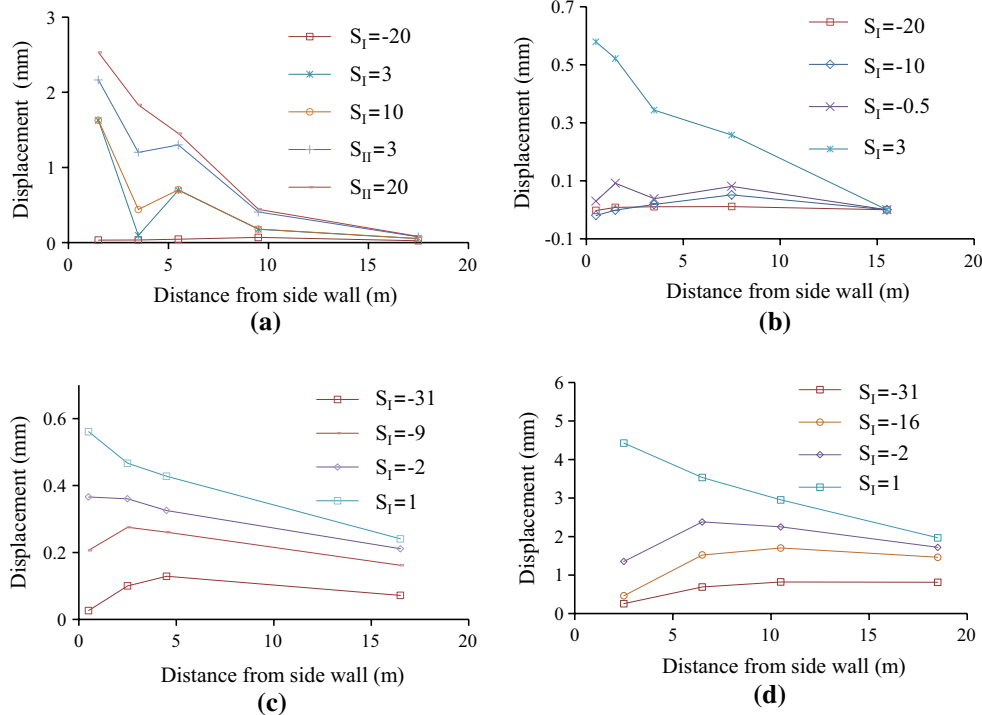


Fig. 22 Multi-modality distribution characteristic of the displacements at the measuring points during the excavation: **a** DSP-01-T, **b** DSP-01-M, **c** DSP-02, **d** DSP-03 (S_I is the distance between the

monitoring section and the upper pilot working face, while S_{II} is the distance between the monitoring section and the working face excavation of the upper side wall)

depth successively showed a reducing trend at DSP-01-M, DSP-02, DSP-03 and DSP-01-T. Located in the fault zone, the integrity of the rock masses at DSP-04 was the poorest; moreover, the displacement and effect of depth at DSP-04 were the biggest among all laboratories. For each multi-point extensometer, the final displacement at the nearest point was largest and decreased gradually along the radial direction of the tunnel.

Unlike the final displacement, which always decreased along the radial direction, the intermediate displacements of the measurement points at different depths showed a much more complex spatial distribution during the excavation. Specifically, the displacements at measurement points located far from the side wall were larger than those near the side wall at certain excavation stages. Thus, an approximate multi-modal distribution characteristic could be observed, as shown in Fig. 22. The multi-modality distribution

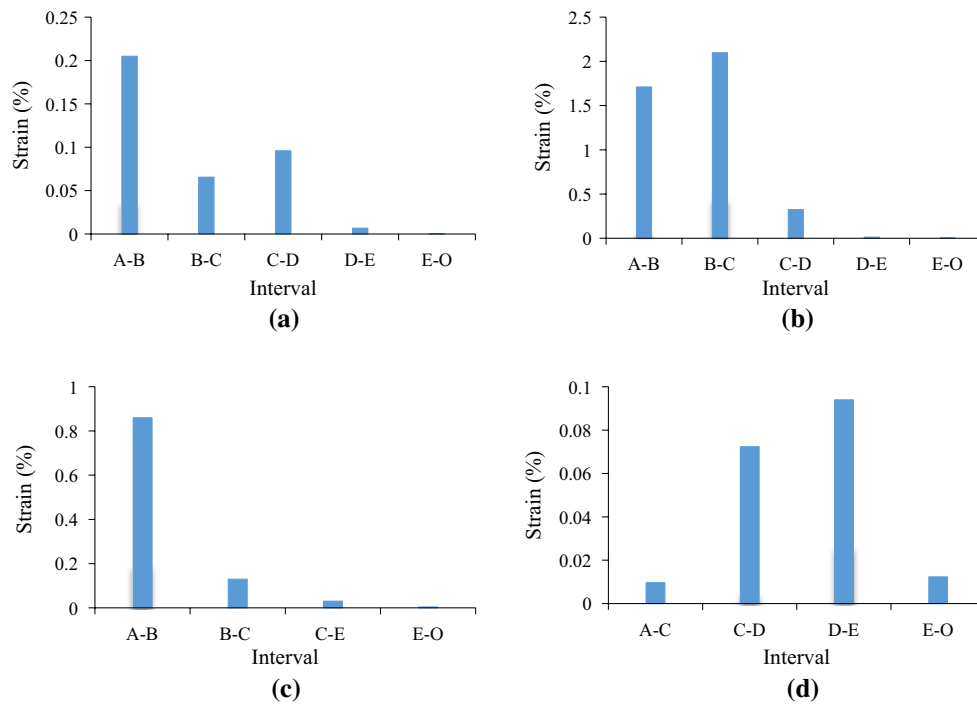


Fig. 23 Distribution characteristics of the strain obtained after the excavation: **a** DSP-01-T, **b** DSP-01-M, **c** DSP-02, **d** DSP-03

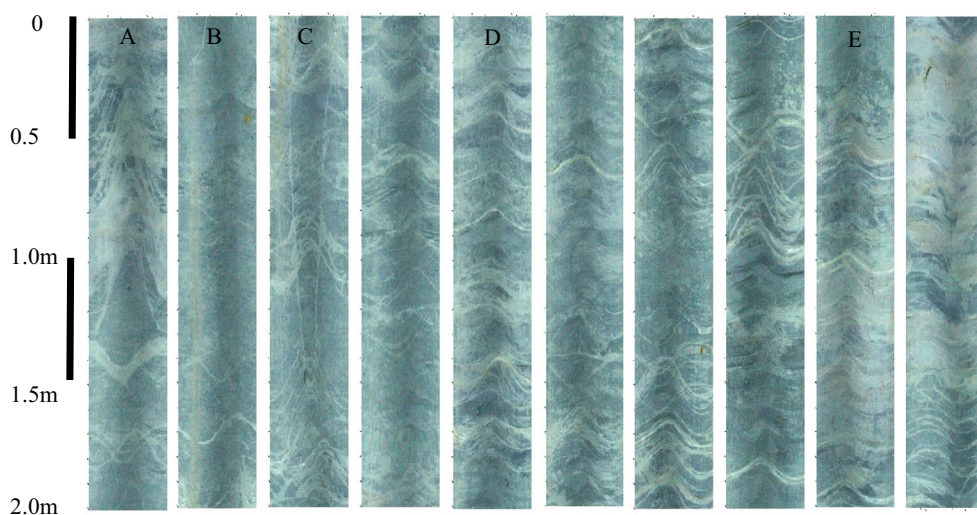


Fig. 24 Test result of DSP-01-T borehole before excavation using digital borehole camera. Images show every 2-m interval from borehole bottom (A, B, C, D and E are measurement points)

characteristic appeared mostly during the excavation of the upper pilot tunnel. Taking DSP-02 as an example (Fig. 22c), when S_1 , the distance between the monitoring section and the upper pilot working face, was less than -31 m, the displacements, in decreasing order, were observed at measurement points C, B and A. As the working face gradually approached $S_1 = -9$ m, the displacements showed a reducing trend at points B, C and A. When S_1 was larger than -2 m, the displacements showed a reducing trend at points A, B and C.

After the excavation of the Labs, the final strain, defined as the ratio of relative displacement to the interval length between two measurement points, also exhibited the multimodal distribution characteristic, as shown in Fig. 23. The strain of interval C–D was larger than that of interval B–C in DSP-01-T, whereas in DSP-01-M, the strain of interval

B–C was greater than that of interval A–B. In addition, in DSP-03, the maximum strain was observed in interval D–E, followed by the strains of C–D, E–O and A–C. The sum of the relative displacements of D–E and E–O accounted for 79.61% of the total displacement.

In Figs. 22 and 23, it can be readily observed that the abnormal strain intervals are consistent with the measurement points wherein the displacement presented multimodal distribution characteristics during the excavation, such as points DSP-01-T-C, DSP-01-M-B and DSP-02-C as well as points D and E in DSP-03.

Fig. 25 Distribution of pre-existing cracks before excavation in DSP boreholes: **a** DSP-01-T, **b** DSP-01-M, **c** DSP-02, **d** DSP-03

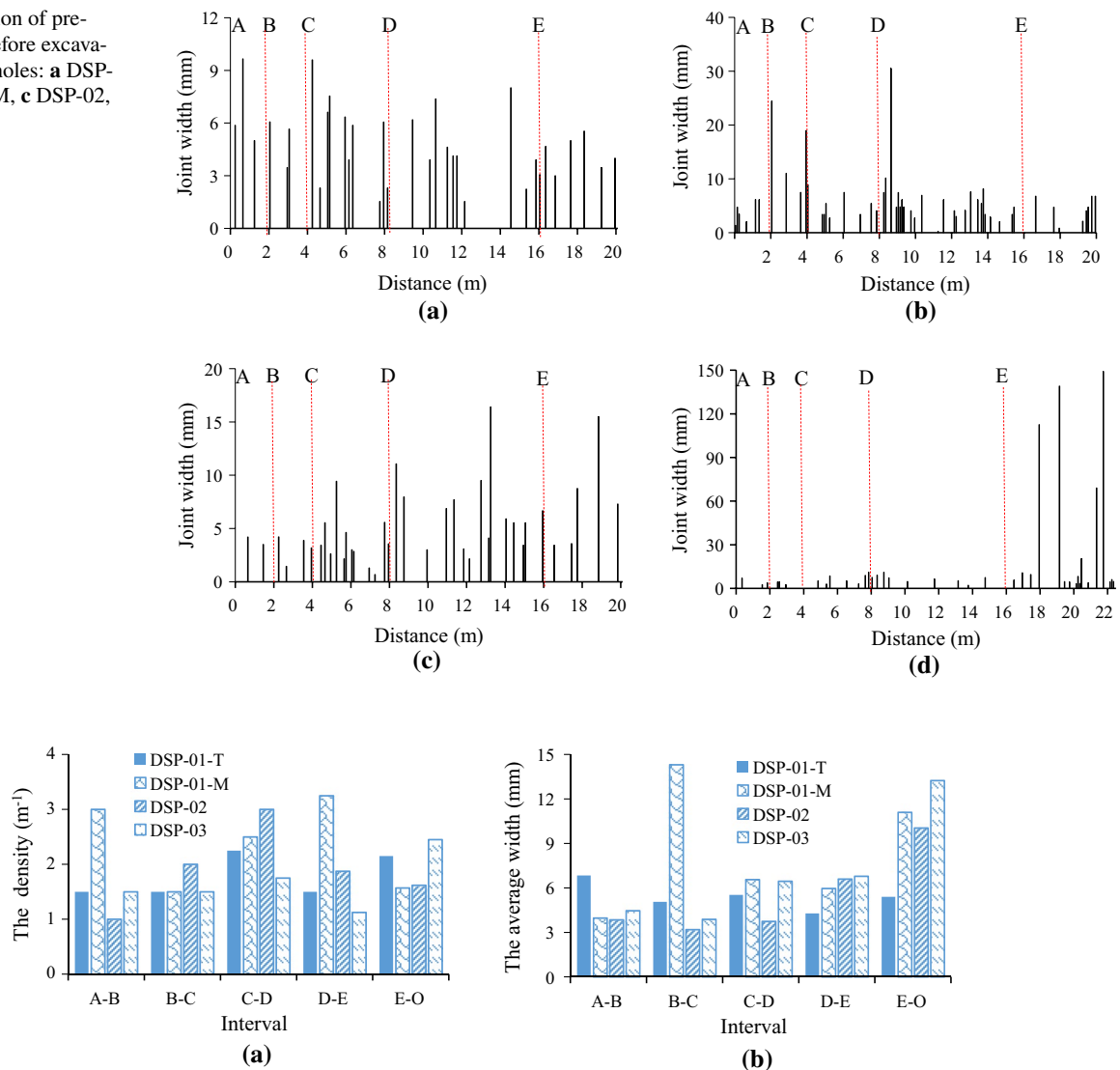


Fig. 26 Densities and average widths of pre-existing cracks before excavation in each measuring point interval: **a** joint density, **b** average joint width

5.2 Analysis of the Mechanism of Internal Displacement Distribution in Surrounding Rock Masses

The typical results obtained for DSP boreholes using digital borehole cameras are shown in Fig. 24. The pre-existing cracks along the axial direction of the boreholes are abstracted and illustrated in Fig. 25. Figure 26 summarises the densities and average widths of the pre-existing cracks in each interval. Although the rock strength of DSP-01-M is greater than those of DSP-02 and DSP-03, the displacement and influence depth of DSP-01-M are still larger than those of DSP-02 and DSP-03 because of the more developed fractures in DSP-01-M, as shown in Fig. 25 and Table 4. In contrast to the multi-modal displacement characteristics shown in Figs. 22 and 23, it was found that the measurement points and intervals with values larger than those of both their neighbours were often associated with more highly developed crack conditions, i.e. wider crack widths or higher crack densities. For example, in DSP-01-T, as seen in Figs. 22a, 23a, 25a and 26a, both the average width and density of the cracks in interval C–D are greater than those in interval B–C. Correspondingly, the strain of interval C–D is larger than that of interval B–C even though B–C is closer to the side wall. Meanwhile, the intermediate displacement at measurement point C after the working face passes the monitoring section with $S_I = 3$ and 10 m during the excavation of the pilot tunnel (and with $S_{II} = 3$ m during the expanding excavation of the upper side wall) is larger than that at point B.

To investigate the effect of joints on the internal displacement behaviour of the surrounding rock, numerical models based on FLAC^{3D} were established. There were used to simulate the excavation process with the surrounding rock divided into zones based on the distribution of joints shown in Fig. 25d. Figure 27 shows the model mesh with the size being $230 \times 100 \times 100$ m in length, width and height, respectively, and a typical observation section (using 5# Laboratory as an example). The initial geostress state is shown in Table 5. To model the brittle yield and breakage of hard rock under high geostress, the rock mass is assumed as elastic–brittle–plastic continuum which yields according to the Mohr–Coulomb yield criterion and permits deterioration of elastic modulus, cohesive strength and internal friction angle according to the yield state of rock indexed by accumulated general plastic strain (Jiang et al. 2008a). The properties of the rockmass, listed in Table 6, were comprehensively back analysed from multi-measurement, including the depth of the excavation damage zone and displacement,

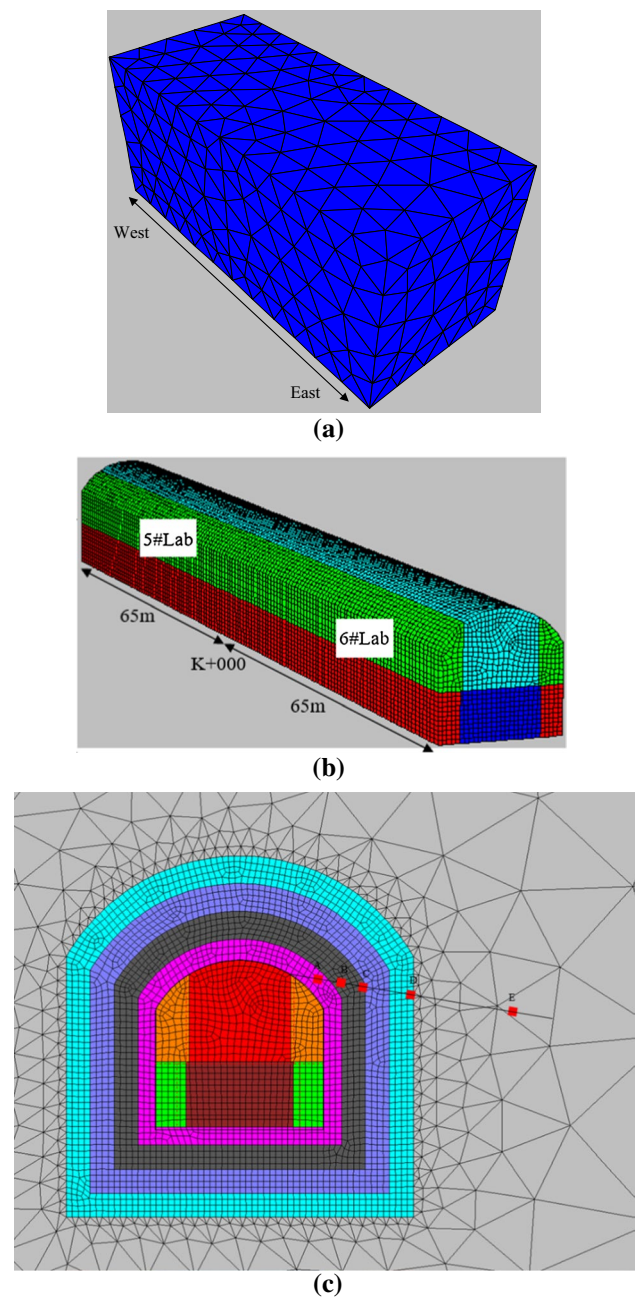


Fig. 27 Numerical model of 5# Lab and the layout of measurement points of DSP-03: **a** numerical model, **b** model mesh, **c** the layout of measurement points of DSP-03

Table 5 Initial geostress conditions in the numerical model

σ_x (MPa)	σ_y (MPa)	σ_z (MPa)	τ_{xy} (MPa)	τ_{yz} (MPa)	τ_{zx} (MPa)
47.86	54.55	62.19	4.52	2.35	15.14

using an intelligent back analysis procedure that has been extensively validated (Feng et al. 2000; Jiang et al. 2008b). The properties of the fractured zones were weakened appropriately to simulate the presence of joints. The simulated excavation stages are similar to construction process. Typical calculated displacements arising during excavation of 5# Lab are shown in Fig. 28. There was good agreement between the calculated and measured results, suggesting that the numerical scheme is an efficient quantitative method in investigating the internal displacement behaviour. Numerical results for 5# Lab were used in the analysis since it has the most significant multi-modal displacement behaviour, with displacement at the inner points (e.g. C) during the excavation process being more than threefold that at the outer points (e.g. A). Figure 29 shows the progress of displacement evolution at the monitoring section of DSP-03 with S_1 being -31 , -16 , -2 , and 1 . The joints were found to play a different role in the displacement behaviour as the working face approached the monitoring section. When the working face was ahead of the monitoring section, and far from it (S_1 is less than -16), the strain near point C was larger than that near point A because the joint near the point C was more developed. That is, a squeezing area then formed between points A and C, as can be seen through larger density of displacement contours in Fig. 29. As a result, the displacement at point C was more than twice of that at point A. As the working face came closer, excavation-induced displacement became increasingly significant, gradually masking the effect of local joints. Displacement at point A became approximately equal to that at C when S_1 was -2 and significantly exceeded it when the working face passed ($S_1 = 1$). Finally, the displacement distribution returned to typical convergence behaviour with the displacement decreasing from point A to point E.

In summary, when the working face is far from the monitoring section, the disturbance intensity at each measurement point is similar; therefore, the integrity (i.e. the crack conditions) of the rock masses becomes the main factor influencing displacement. In this case, the weaker the integrity

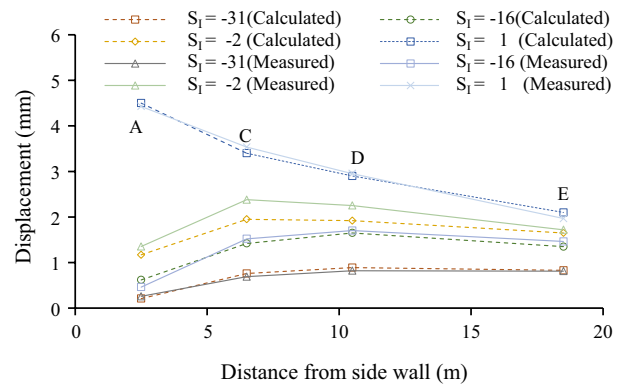


Fig. 28 Comparison of calculated and measured displacement at measurement points of DSP-03 in 5# Lab (S_1 is the distance between the monitoring section and the upper pilot working face)

of the rocks, the larger the displacement. Meanwhile, there is no open surface at the mounting section; therefore, the multi-modality distributions of strain and displacement may appear when rock masses far from the side wall are less intact than those near the side wall. Nevertheless, when the working face approaches the monitoring section, the measurement points near the side wall are influenced more significantly than those farther away. Meanwhile, the rock integrity near the side wall decreases and the lateral confinement of the side wall essentially disappears. As a result, the displacement at points near the side wall increases more than that at points far from the side wall. Subsequently, the multi-modality distribution of displacement essentially disappears; however, the displacements in the fracture-development intervals are still large and thereby result in the continued existence of a multi-modality distribution for strain.

Table 6 Basic mechanical parameters of the rockmass

Elastic modular (GPa)	Original rockmass	12.66
	Yield rockmass (residual)	7.85
	Fractured zones	1.35
Cohesion strength (MPa)	Original rockmass	22.68
	Yield rockmass (residual)	6.84
	Fractured zones	3.10
Internal friction angle (°)	Original rockmass	27.4
	Yield rockmass (residual)	48.0
	Fractured zones	22.0
Critical general plastic strain (10^{-3})	Corresponding to residual cohesion strength	4.0
	Corresponding to residual internal friction angle	6.0
Tension strength (MPa)		1.5

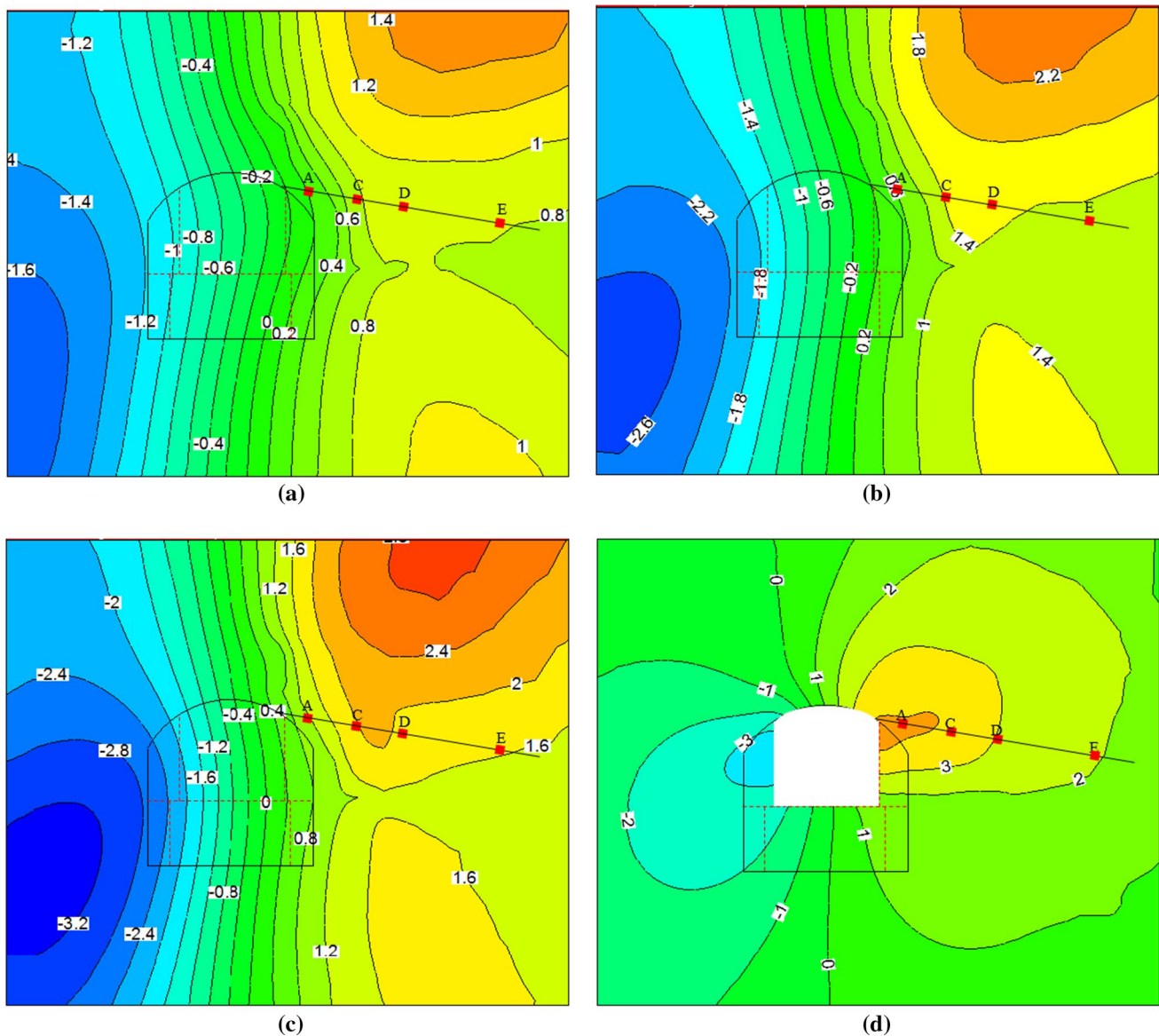


Fig. 29 Calculated displacement at measurement points DSP-03 in 5# Lab with different distance from working face: **a** $S_1 = -31$, **b** $S_1 = -16$, **c** $S_1 = -2$, **d** $S_1 = 1$

6 Conclusions

A comprehensive experimental scheme that included pre-installed continuous-recording multi-point extensometers, acoustic velocity testing and a digital borehole camera was adopted at CJPL-II, which was subjected to an overburdened depth of 2,400 m and excavated layer-by-layer using the drilling and blasting method. The evolution of the associated displacement of hard surrounding rock masses and the damage caused to them during the entire excavation process of the subjected tunnel (under high-stress conditions) was ultimately obtained.

A new method of classifying displacement evolution characteristics was presented in this study by analysing such characteristics at each measurement point during two adjacent blasting processes. With regard to the classification method, the time-dependent evolution characteristics of the displacements of the surrounding rock masses can be divided into four types, influenced by the combined effects of rock strength, degree of excavation disturbance and stress state. The results indicate that the displacement increase in C-type was dominant and that the worse the integrity of the rock mass, the greater the proportion of the displacement increase in C-type. Moreover, the width and density

of pre-existing cracks can affect the distribution of displacements as well as the predominant strain levels within deep hard-rock tunnels. Owing to the heterogeneity of rock masses, such displacements and strain levels may exhibit a multi-modal distribution characteristic.

The multi-modal distribution characteristic of displacement at measurement points is usually obtained before the working face passes the monitoring section. Therefore, it is difficult to obtain this characteristic unless the displacement-monitoring equipment is pre-installed. Research methods and conclusions associated with multi-modal distribution characteristics can provide sound bases and references for a comprehensive study on deep cracking and zonal disintegration of surrounding rock masses. Based on the analyses of the displacement evolution characteristics depicted in this study, one can successfully determine the fracture evolution process of the surrounding rock. Subsequently, one can evaluate the effects of tunnel excavation and support systems as well as deterministically characterise a tunnel's overall stability.

Acknowledgements The authors acknowledge the financial support from the National Natural Science Foundation of China under Grant Nos. 41320104005, 51621006 and 51579043 and the State Key Research Development Programme of China (Grant No. 2016YFC0600702). The authors thank Professors Jimin Wang and Xionghui Zeng, Dr. Kai Jiao, Jifang Zhou, Mr. Yuan Cheng who gave support and assistance in situ monitoring at CJPL-II.

References

- Andersson JC, Martin CD (2009) The Äspö pillar stability experiment: part I—experiment design. *Int J Rock Mech Min Sci* 46(5):865–878
- Andersson JC, Martin CD, Stille H (2009) The Äspö pillar stability experiment: part II—rock mass response to coupled excavation-induced and thermal-induced stresses. *Int J Rock Mech Min Sci* 46(5):879–895
- Feng XT, Zhang ZQ, Sheng Q (2000) Estimating mechanical rock mass parameters relating to the Three Gorges Project permanent shiplock using an intelligent displacement back analysis method. *Int J Rock Mech Min Sci* 37(7):1039–1054
- Feng XT, Yu Y, Feng GL, Xiao YX, Chen BR, Jiang Q (2015) Fractal behaviour of the microseismic energy associated with immediate rockbursts in deep, hard rock tunnels. *Tunn Undergr Space Technol* 51:98–107
- Feng XT, Zhang CQ, Qiu SL, Zhou H, Jiang Q, Li SJ (2016a) Dynamic design method for deep hard rock tunnels and its application. *J Rock Mech Geotech Eng* 8(4):443–461
- Feng XT, Wu SY, Li SJ, Qiu SL, Xiao YX, Feng GL, Shen MB, Zeng XH (2016b) Comprehensive field monitoring of deep tunnels at Jinping underground laboratory (CJPL-II) in China. *Chin J Rock Mech Eng* 35(4):649–657 (in Chinese)
- Hansmire WH (1978) Suggested methods for monitoring rock movements using borehole extensometers. *Int J Rock Mech Min Sci* 15(6):305–317
- Hibino S, Motojima M (1995) Characteristic behaviour of rock mass during excavation of large scale caverns. In: Fujii T (ed) Proceedings of the 8th international congress on rock mechanics of the international society for rock mechanics. Balkema, Rotterdam, pp 583–586
- Hibino S, Motojima M, Kanagawa T (1993) Rockmass behavior during large-scale cavern excavation. In: Hudson JA (ed) Comprehensive rock engineering. Pergamon, London, pp 631–651
- Hoek E, Brown ET (1980) Underground excavations in rock. The Institution of Mining and Metallurgy, London
- Huadong Engineering Corp. Ltd. (2014) Design handbook of China Jinping underground laboratory, Hangzhou (in Chinese)
- Huang RQ, Huang D, Duan SH, Wu Q (2011) Geomechanics mechanism and characteristics of surrounding rock mass deformation failure in construction phase for underground powerhouse of Jinping I hydro-power station. *Chin J Rock Mech Eng* 30(1):23–35 (in Chinese)
- Hudson JA, Cosgrove JW, Kemppainen K, Johansson E (2011) Faults in crystalline rock and the estimation of their mechanical properties at the Olkiluoto site, western Finland. *Eng Geol* 117(3–4):246–258
- Jiang Q, Feng XT, Chen GQ (2008a) Study on deterioration model for hard rockmass under high geo-stress. In: Fan JH, Chen HB (eds) Advance in heterogeneous material mechanics 2008. China, pp 1108–1112
- Jiang Q, Feng XT, Su GS, Chen CQ (2008b) Intelligent back analysis of rock mass parameters for large underground caverns under high earth stress based on EDZ and increment displacement. *Chin J Rock Mech Eng* 26(1):2654–2662 (in Chinese)
- Li SJ, Feng XT, Wang CY, Hudson JA (2013) IRSM suggested method for rock fractures observations using a borehole digital optical televiewer. *Rock Mech Rock Eng* 46(3):635–644
- Malan DF (1998) Investigation into the identification and modelling of time-dependent behaviour of deep level excavations in hard rock. Dissertation, University of Witwatersrand
- Malan DF (1999) Time-dependent behaviour of deep level tabular excavations in hard rock. *Rock Mech Rock Eng* 32(2):123–155
- Martino JB, Chandler NA (2004) Excavation-induced damage studies at the underground research laboratory. *Int J Rock Mech Min Sci* 41(8):1413–1426
- Nadimi S, Shahriar K, Sharifzadeh M, Moarefvand P (2011) Triaxial creep tests and back analysis of time-dependent behavior of Siah Bisheh cavern by 3-dimensional distinct element method. *Tunn Undergr Space Technol* 26(1):155–162
- Posiva (2009) Olkiluoto site description, 2008. Parts 1 and 2, Posiva report 2009-01, pp 714. www.posiva.fi
- Siren T, Hakala M, Valli J, Kantia P, Hudson JA, Johansson E (2015) In situ, strength and failure mechanisms of migmatitic gneiss and pegmatitic granite at the nuclear waste disposal site in Olkiluoto, Western Finland. *Int J Rock Mech Min Sci* 79:135–148
- Takahashi T, Takeuchi T, Sassa K (2006) ISRM suggested methods for borehole geophysics in rock engineering. *Int J Rock Mech Min Sci* 43(3):337–368
- Wei JB, Deng JH, Wang DK, Cai DW, Hu JZ (2010) Characterisation of deformation and fracture for rock mass in underground powerhouse of Jinping I hydropower station. *Chin J Rock Mechan Eng* 29(6):1198–1205 (in Chinese)
- Xiao YX, Feng XT, Li SJ, Feng GL, Yu Y (2016) Rock mass failure mechanisms during the evolution process of rockbursts in tunnels. *Int J Rock Mech Min Sci* 83:174–181
- Zareifard MR, Fahimifar A (2016) Analytical solutions for the stresses and deformations of deep tunnels in an elastic–brittle–plastic rock mass considering the damaged zone. *Tunn Undergr Space Technol* 58:186–196